Catalytic Reduction of NOx With NH3 Over CeO2 and SiO2 Supported Tungstophosphoric Acid: Promoting Effects of Ceria Support and Cobalt Proton Substitute

Imane El Arrouji, Jamil Toyir, Cherif Larabi, Kai Szeto, Aimery De Mallmann, Mostafa Taoufik, Abdallah Oulmekki

Catalytic reduction of NO_x with NH_3 over CeO_2 and SiO_2 supported tungstophosphoric acid: promoting effects of ceria support and cobalt proton substitute.

Imane El Arrouji [*] [1,3], Jamil Toyir [2], Cherif Larabi [3], Kai C. Szeto [3], Aimery de Mallmann [3], Mostafa Taoufik [3] and Abdallah Oulmekki [1]

[1] Laboratoire des Procédés, Matériaux et Environnement (LPME), Faculté des Sciences et Techniques de Fès, université Sidi Mohammed Ben Abdellah, BP. 2202 Morocco.

[2] Laboratoire des Procédés, Matériaux et Environnement (LPME), Université Sidi Mohammed Ben Abdellah, FP-Taza, B.P 1223, Morocco.

[3] Université Lyon 1, Institut de Chimie Lyon, CPE Lyon CNRS, UMR 5128 CP2M, LCOMS, 43 Bd du 11 Novembre 1918, 69616 Villeurbanne Cedex, France.

*Corresponding author:

E-mail address: imane.elarrouji@usmba.ac.ma (Imane El Arrouji)

Abstract

Grafted tungstophosphoric acid ($H_3PW_{12}O_{40}$/ HPW) is applied as a catalyst in the selective catalytic reduction of NO_x with NH_3 (NH_3-SCR). The HPW/CeO_2 catalyst has been found to be effective in the SCR reaction compared to HPW/SiO_2. The cobalt-exchanged HPW/CeO_2 improved NO_x conversion, which reached 98% over a wide operating temperature window (280-500 °C). The better NO_x performance of the CoPW/CeO_2 catalyst is mainly due to the higher dispersion of tungsten on the CeO_2 support, the formation of oxygen vacancies and the production of nitrogenous species. Incorporation of vanadium decreased the acidity of HPW, which reduced SCR activity on the HPVW/CeO_2 catalyst.

Keywords Tungstophosphoric acid. DeNO_x. Ceria. Cobalt. Dispersion capacity. Oxygen vacancies.

1 Introduction

Nitrogen oxides (NO_x) are principally generated during fossil fuel combustion at high temperatures. The harmful NO_x gases emitted from vehicles, power stations, and industrial boilers represent a major source of atmospheric pollution with serious impacts on the environment and human health [1]. To cope with the serious issue, several regulations have been proposed to control the NO_x emissions [2]. Currently, selective catalytic reduction with ammonia (NH_3-SCR) is one of the attractive processes for NO_x abatement, applied in both stationary and mobile sources.

Development of highly effective catalyst is a key component for SCR-deNO_x technology. The most commercially catalysts used are the V_2O_5-MO_3/TiO_2 (M = W, Mo). Although the NO_x conversion of these systems are acceptable [3,4], some issues detected have limited their applications in mobile operations (diesel vehicles), notably, poor N_2 selectivity, toxicity of vanadic species, low thermal stability and high oxidation of SO_2 to SO_3 [5-7]. Several types of catalytic systems are investigated, particularly, Cu/Fe-Zeolite [8], rare-earth-based compounds [9] and metal oxides [10], which revealed a remarkable improvement in the NO_x reduction. Ceria (CeO_2) has been used successfully as support for catalysts in NH_3-SCR reaction due to its good reducibility, capacity to store oxygen

and high SO_2 tolerance [11]. However, ceria alone had a mediocre catalytic activity [12,13]. Adding transition metal oxides such as WO_3, MnO_x, ZrO_2 and TiO_2 to ceria greatly improves $deNO_x$ activity, this beneficial effect was explained by promoting effects of metals on CeO_2 redox, acid and thermal properties inside these multifunctional systems [14–17]. Interesting results are obtained on theses catalysts so far, however not reaching a full $deNO_x$ performance.

Polyoxometalates (POMs) of the keggin type as potential providers of transition metals to boost the required properties of support in SCR catalysts are known as metal-oxygen clusters. They are sub-categorized in heteropolyacids (HPAs) and heteropolysalts (HPSs) [18]. In their structure, it is easy to substitute the proton and/or metallic atoms (tungsten) by the lower valence transition metals such as V^{5+}, Co^{2+}, Cu^{2+}, Fe^{2+}... etc. [19]. Based on well-defined metals mixture, POMs may exhibit an outstanding acid and redox properties, which makes them suitable catalysts for bifunctional reactions. For example, tungstophosphoric acid supported on γ-Fe_2O_3 enhances the activity function of the support at high temperature. It is shown that the ability of γ-Fe_2O_3 to adsorb NH_3 is improved with HPW grafting, inducing excellent SCR activity at 250-500 °C [20]. Tungstophosphoric ($H_3PW_{12}O_{40}$), silicotungstic ($H_4SiW_{12}O_{40}$) and molybdophosphoric ($H_3PMo_{12}O_{40}$) acids modified CeO_2 have been tested as well in the SCR reaction. It is reported that the high $deNO_x$ activity obtained for these catalysts is mainly due to the introduction of HPAs, which in fact, promotes the redox properties and increase the amount of Brønsted acid sites on the surface of CeO_2 [21-23]. Herein, there can be an opportunity to develop another POM-type catalyst with great catalytic activity for selective catalytic reduction with ammonia.

In the present investigation, POMs-based catalysts are prepared using ceria and silica supports in interaction with various heteropolysalts and heteropolyacids. The catalytic performance of tungstophosphoric acid (HPW) in the NH_3-SCR reaction, was first measured separately with the support. Afterwards, the effect of proton and tungsten-content on the SCR catalytic performance of HPW/CeO_2 catalysts was also evaluated. The physicochemical and structural properties of the catalysts are analyzed by N_2 physisorption (BET), Scanning electron microscopy (SEM), X-ray diffraction, Infrared, Raman, and UV-Vis diffuse reflectance spectroscopic methods. Based on this characterization, structure-activity relationships have been established.

2 Experimental section

2.1 Characterization methods

The elemental and chemical composition of the catalysts was performed by means of Energy Dispersive X-Ray Analysis using a FEI-quanta 200 instrument. Catalysts surface area measurements were conducted on Micromeritics ASAP 2020 using nitrogen adsorption at 77 K. Before, the samples were outgassed at 200 °C for 4 h. The surface morphology of catalysts was analyzed on a FEI-quanta 200 instrument, operated at 20 KeV. X-ray diffraction (XRD) was conducted on Bruker D8 Advance diffractometer using Cu Kα (λ=1.5406 Å) radiation functioned at 40 kV and 40 mA. The patterns were recorded in the angle range between 5 and 90°. The lattice parameters refinement was collected according to the Rietveld method via High-Score Plus software using (JCPDS: 34-0394) as reference. The average crystallite sizes (d_{XRD}) were estimated with the Scherrer equation. Infrared spectroscopy (FT-IR) was measured on a JASCO-FTIR 4200 spectrometer in the Mid-infrared region. The spectra were analyzed from 400 to 4000 cm^{-1} with 4 cm^{-1} resolution and 64 scan number. Raman spectroscopy was carried out on LabRAM HR Evo spectrometer equipped by a green laser diode functional at λ = 785 nm. The

data was collected between 100 and 1500 cm^{-1} at room temperature, the integration time was 20 s and the scan numbers were 16. UV-Vis diffuse reflectance spectroscopy was executed on a PerkinElmer Lambda 900 spectrometer. The compounds were recorded in range of 190-850 nm with the presence of $BaSO_4$ as a reference. The energy gaps (Eg) were estimated from Tauc plot in directly transition. X-ray photoelectron spectroscopy (XPS) spectra of ceria, HPW/CeO_2 and CoPW/CeO_2 were recorded on Axis Ultra Kratos spectrometer with Al Kα (1486.6 eV) radiation. The calcined compounds were evacuated and maintained at residual pressure in the ion-pumped analysis chamber below 1.33 10^{-8} mbar (1 mbar = 101.33 Pa) during data acquisition. The binding energies of spectra were calibrated using the photoemission peak C 1s at 284.9 eV. The surface atomic percentage of each species was estimated by calculating the integral of each peak after subtraction background and fitting the experimental curve to a Gaussian model.

2.2 Preparation of catalysts

Three POMs types were prepared and supported on ceria (from Solvay) and silica (aerosil 200/ from Evonik). HPW acid is a commercial product obtained from Sigma Aldrich. Tungsto-vanado-phosphoric acid ($H_4PW_{11}VO_{40}$/ HPVW) generated from the substitution of tungsten by vanadium in HPW was prepared following the procedure described in previous works [24]. First, A stoichiometric mixture of Na_2HPO_4,$2H_2O$ and $NaVO_3$ was dissolved in water, then, acidified with H_2SO_4. In a second step, a solution of Na_2WO_4,$2H_2O$ was added dropwise to the starting mixture. The pH was adjusted to ~1.5 by H_2SO_4. Thus, the suspension was extracted with diethyl ether and preserved at 4°C. The crystals were obtained after 5 days. For HPW modified by the transition metals (heteropolysalts/ $M_{1.5}PW_{12}O_{40}$, M= Fe, Co, Cu and Zn), $Ba(OH)_2$ solution was introduced into HPW to neutralize the protons. The barium salt was obtained first. Next, MSO_4 (M= Fe, Co, Cu and Zn) was slowly added to precipitate, barium sulfate $BaSO_4$ and heteropolysalts were recovered [25]. HPW/CeO_2 or SiO_2, HPWV/CeO_2 and MPW/CeO_2 (M= Fe, Co, Cu and Zn) catalysts were prepared via wet impregnation method. The appropriate amount of ceria/ silica was added onto the POMs (9 wt % amount of tungsten) in ethanol solution. Afterwards, the mixture was stirred for 4 h at room temperature. Then, the excess of solvent was evacuated using a rotary evaporator at 30 °C and then, the dry solids were calcined at 500 °C for 3h under air. The elemental analysis of all catalysts using EDX indicated the presence of ca. 9 wt% W (Table S1).

2.3 Catalytic activity

NH_3-SCR catalytic activity was conducted in a fixed-bed quartz reactor. The reaction mixture was composed of 300 ppm NO, 350 ppm NH_3 and 10 vol % O_2 with a total flow rate of 300 mL min^{-1} (GHSV = 30000 h^{-1}). For each test, 30 mg of catalyst diluted in silicon carbide (SiC) was loaded into the reactor. The reaction is carried out in the temperature range from 50°C to 600°C with a heating rate of 10 °C/ min. The concentration of the outlet gases (NO, NO_2, N_2O and NH_3) is continuously analyzed by Antaris IGS FTIR (Thermo-Fischer) equipped with a gas cell of 200 mL. The equations (1, 2 and 3) have been adopted to calculate NO conversion, N_2 selectivity and N_2 yield.

$$NO_{conversion}(\%) = \frac{[NO]_{in}-[NO]_{out}-[NO_2]_{out}}{[NO]_{in}} \times 100 \qquad \text{(Eq. 1)}$$

$$N_{2_{selectivity}}(\%) = \frac{[NO]_{in}+[NH_3]_{in}-[NO_x]_{out}-[NH_3]_{out}-2\,[N_2O]_{out}}{[NO]_{in}+[NH_3]_{in}-[NO_x]_{out}-[NH_3]_{out}} \times 100 \quad \text{(Eq. 2)}$$

$$N_{2_{yield}}\ (\%) = NO_{conversion} \times N_{2_{selectivity}} \quad \text{(Eq. 3)}$$

NH_3-SCR was further investigated to determine the reaction kinetic parameters using the polyoxometalates based catalyst. The SCR was generally controlled by a first-order reaction with a strong dependence on NO concentration [26]. The kinetic parameters were calculated in a differential regime (NO conversion less than 20%) according to Eq. 4:

$$k = \frac{F_0}{W} \ln\left(\frac{1}{1-X_{NO}}\right) \text{(mol g}^{-1}\text{ s}^{-1}\text{)} \quad \text{(Eq. 4)}$$

For each catalyst the activation energy (E_a) is estimated from the Arrhenius plot through the following equation (Eq. 5):

$$\ln k = \ln A - \frac{E_a}{RT} \quad \text{(Eq. 5)}$$

Where k is the rate constant, F_0 is the gas flow, W is the mass of catalysts, X_{NO} is the NO conversion and A is the pre-exponential factor.

3 Results

3.1 Characterization of the catalysts

Textural parameters of catalysts and dispersion capacity are listed in Table 1 and Fig. S1. Initial values of the support BET surface aera (S_{BET}) were 247 and 200 $m^2\ g^{-1}$ for ceria and silica, respectively. After addition of CoPW, HPW and ZnPW into support, S_{BET} slightly decreased. Similar effect was observed for average pore volume. However, when FePW, CuPW and HPVW were grafted onto the CeO_2 support, a drastic decrease in the surface parameters has been noticed. It is apparent that the catalysts surface area is correlated with the tungsten dispersion capacity. This dispersion followed the same trend as that detected for S_{BET} of the catalysts. As shown in Fig. S1. The catalysts kept similar type isotherm to those of the supports. Ceria-based catalysts showed V-type isotherms and H2-type hysteresis with a relative pressure in 0.5-0.8 range. While, HPW/SiO_2 is classified as type IV isotherm corresponding to H3 hysteresis loop and relative pressure around 0.8-1 interval. The average pore size of the samples was centered in the mesoporous range 3.07-20.76 nm.

Table 1 Textural parameters of catalysts, tungsten dispersion capacity, oxygen vacancies and average particle size

catalysts	S_{BET} ($m^2\ g^{-1}$)	Pore volume ($cm^3\ g^{-1}$)	average pore diameters (nm)	[1]Dispersion capacity (D_C) (mmol of W m^{-2})	[1] Oxygen vacancies I_{600}/ I_{458}	[3] d_{XRD}(Å)
CeO_2	247	0.18	3.07	-	0.016	43
SiO_2	200	0.86	16.45	-	-	-
HPW/ SiO_2	167	0.82	20.76	-	-	-
HPW/ CeO_2	141	0.18	3.73	0.8	0.036	49
CoPW/ CeO_2	174	0.18	3.94	1	0.04	56
FePW/ CeO_2	79	0.12	4.26	0.45	0.024	71
CuPW/ CeO_2	81	016	5.73	0.46	0.030	54
ZnPW/ CeO_2	136	0.18	3.72	0.77	0.032	48
HPVW/ CeO_2	61	0.1	4.38	0.35	0.029	69

[1] Calculated by $Dc = \frac{S_{BET}}{N_A \cdot a^2}$ according to the "Incorporation Model"[27] (where S_{BET} is the surface specific area, N_A Avogadro number and a is the lattice parameter)
[2] Ratio of peak intensities at 600 cm^{-1} and 458 cm^{-1} in Raman spectra.
[3] Crytallite size average determined using Debye-Sherrer equation

The surface morphology of samples and grain size distributions are shown in Fig. 1 a-l and Fig. S2. From the SEM image, it can be clearly seen that the ceria has a homogeneous morphology with a non-uniform particle size distribution (Fig. 1 a). CeO_2 surface is formed by spherical grains with an average diameter of around 1.14 µm (Fig. S2). Regarding the surface porosity, ceria displayed an intra-granular microporosity, which is in accordance with the literature [28,29]. As noticed, the catalysts exhibited a different morphology compared to the CeO_2 support. Grafting of HPW, CoPW and ZnPW into CeO_2 makes the surface more granular (Fig. 1 b, c and f). Indeed, the average particle size is found to be around 1.19, 1.17 and 1.3 µm for HPW/CeO_2, CoPW/CeO_2 and ZnPW/CeO_2, respectively. It should be noted that the grain size of these samples is larger than that of the ceria. However, CeO_2 surface porosity in the catalysts remains unaffected. For MPW/CeO_2 (M = Fe, Cu) and HPVW/CeO_2 (Fig. 1 d, g and l), intense agglomeration was observed. A significant increase in surface particle sizes appears when MPW (M = Fe, Cu) and HPVW grafted onto ceria.

SEM micrograph of silica showed a uniform structure (Fig. 1 h). The surface was found to have a wafer morphology and inter-particle nanopores that are difficult to observe. Once HPW was immobilized (Fig. 1 l), white aggregates with an average size of 0.31 µm appeared on the silica surface. It is suggested that these aggregates are the WO_3 nanoparticles.

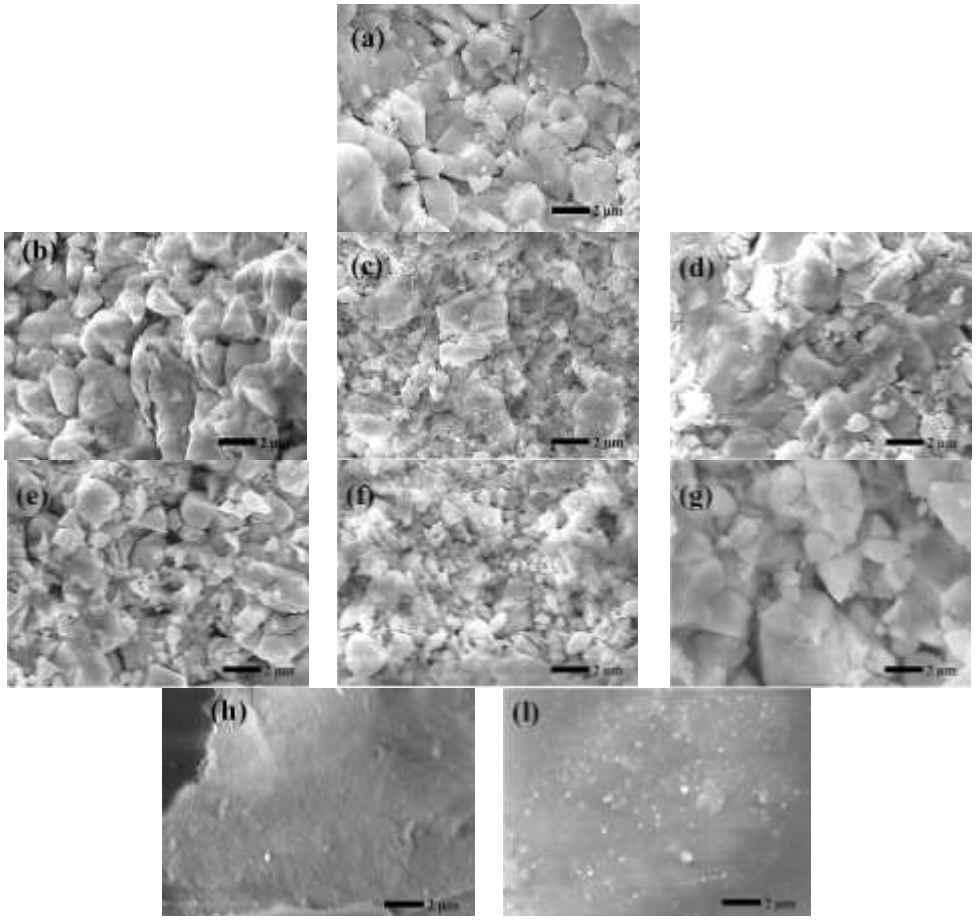

Fig. 1 SEM micrographs of **(a)** CeO_2, MPW/CeO_2 (M= **(b)** H, **(c)** Co, **(d)** Fe, **(e)** Cu, **(f)** Zn), **(g)** HPVW/CeO_2, **(h)** SiO_2 and **(l)** HPW/SiO_2

To know the overall structure and phases nature of the catalysts, powder X-ray diffraction measurements are performed, and the patterns are exposed in Fig. 2 and Fig. S3. Phosphotungstic acid (HPW) bulk (lower in green in Fig.3) revealed a triclinic structure P-1 typic of keggin framework (JCPDS: 50-0304). The intense peaks at 2θ = 7.9°, 8.7°, 10.4°, 17.7°, 20.7°, 23.1°, 25.2°, 31.1°, 34.5° and 37.5° indexed to the diffraction lines (001), (110), (01-1), (10-1), (201), (20-2), (11-3), (22-3), (222), (331) and (15-3) respectively. The distinctive triclinic peaks of HPW are not modified in heteropolysalts and $H_4PW_{11}VO_{40}$ compounds. The catalysts (Fig. 2 a) are principally consisted by the fluorite cubic structure of CeO_2 (JCPDS: 34-0394). The peaks occurring at 2θ = 28.1°, 33.2°, 47.4°, 52.2°, 56.3° and 69.5° are assigned respectively to (111), (200), (220), (311), (222) and (400) reflections. There were no other peaks associated to the keggin structure that could be clearly identified. Compared the refined lattice parameters (Fig. S4, Table S2), it can be seen that the catalysts unit cells values were quite similar to that of the ceria. In addition, no shift observed on the X-ray diffraction lines in the catalysts compared to the ceria support. According to Debye-Scherrer equation, all samples showed higher grain size than ceria support (Table 1).

Silica support showed a broad peak revealing its amorphous nature. Upon HPW impregnation, weak WO_3 peaks at 2θ = 22.6°, 23.3°, 24°, 28°, 33°, 33.9°, 41.5°, 49.8°, 50° and 55° were observed (JCPDS: 96-101-0619).

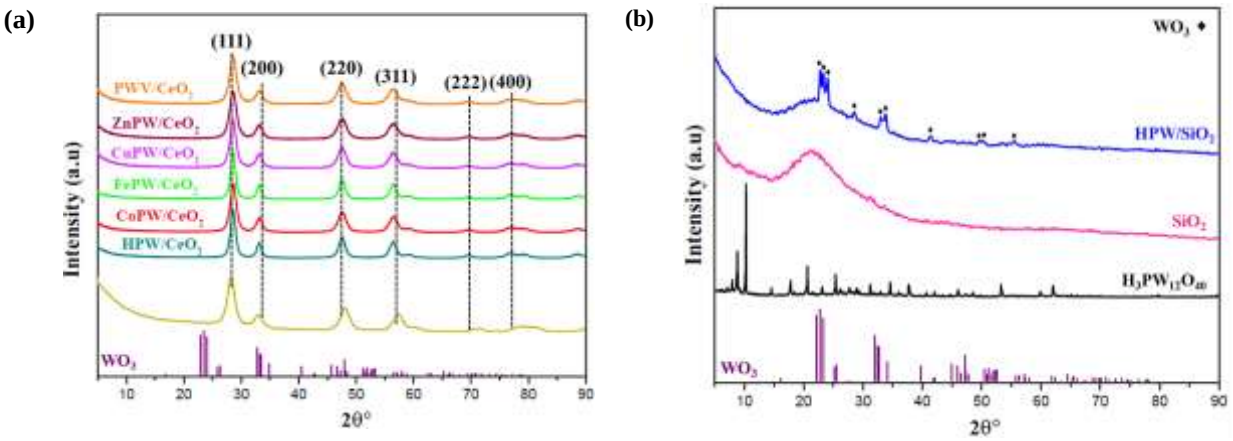

Fig. 2 X-ray diffraction spectra of **(a)** CeO_2, MPW/CeO_2 (M= Co, Fe, Cu, Zn), HPVW/CeO_2 and **(b)** SiO_2, HPW/SiO_2

IR spectra of POMs showed four characteristic peaks associated with Keggin structure (Fig. S5). The peaks at 1080, 985, 888 and 805 cm^{-1} are ascribed to symmetric and asymmetric stretching vibrations of ν_s (P-O_a), ν_{as} (W-O_t), ν_{as} (W-O_b-W), and ν_{as} (W-O_c-W) respectively. CeO_2 exhibited one characteristic band at 505 cm^{-1} attributed to the Ce-O vibration (Fig. 3a) [30]. For silica, three strong vibrations observed at 1048, 804 and 450 cm^{-1} correspond to ν_{as} (Si–O–Si), ν_s (Si–O–Si) and ν_{as} (Si-O_t) (t: terminal position), respectively (Fig. 3b) [31]. The Keggin structure vibrations are hardly identified on the grafted catalysts, the IR peaks observed at 960 and 683 cm^{-1} are attributed respectively to the asymmetric stretching vibration of ν_{as} (W=O_t) and ν_{as} (W-O-W) [32].

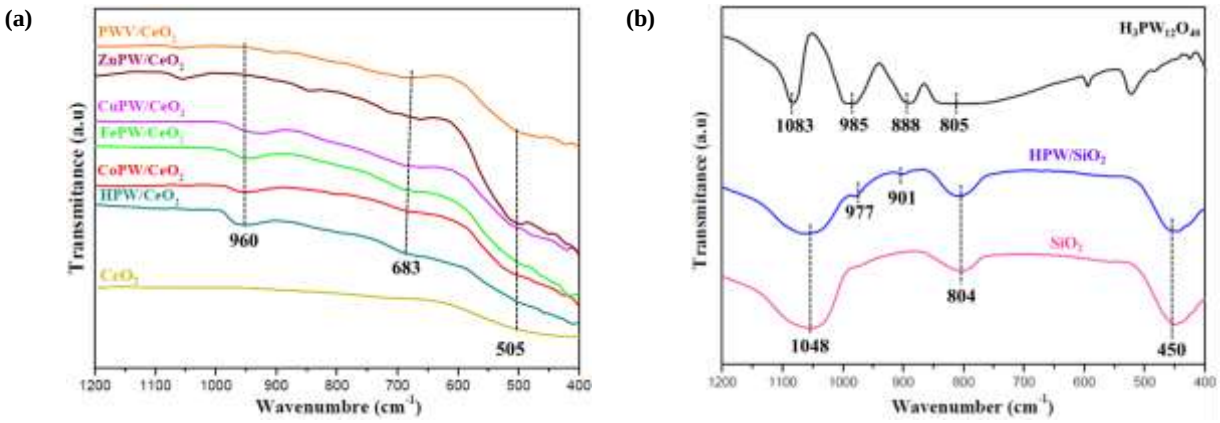

Fig. 3 FT-IR spectra of **(a)** CeO_2, MPW/CeO_2 (M= Co, Fe, Cu, Zn), HPVW/CeO_2 and **(b)** SiO_2, HPW/SiO_2

To analyze more deeply the catalysts structure, Raman technique has been applied with a special attention given to metal oxides present on the ceria surface. The representative Raman spectra of the compounds are showed in Fig 4. POMs exhibited the Keggin skeleton bands at 994 (ν_{as} (W^{I}-O_t)), 978 (ν_{as} (W^{II}-O_t)), 884 (ν_{as} (P-O_a)), 596 (ν_{as} (W-O_b-W)) and (ν_{as} (W-O_c-W)) (Fig. S6). The pure ceria showed an intense band at 458 cm^{-1} ascribed to F_{2g} modes of the cubic fluorite structure. This band is characteristic of the symmetric stretching vibration of O-Ce-O bond [33]. The bands at 261 and 600 cm^{-1} indicate the presence of the oxygen vacancy sites in ceria lattice (Fig. 4a) [34]. All catalysts exhibit bands at around 460, 261 and 591 cm^{-1} ascribed to vibration of cubic ceria. Two novel peaks at 810 and 910-1000 cm^{-1} were detected. The peak at 810 cm^{-1} is due to A_{1g} vibration mode of W-O in polytungstic species (WO_5/WO_6) [35]. Whereas the peaks at 910-1000 cm^{-1} are ascribed to the tungsten terminal groups (W=O_t) characteristic of WO_4 coordination in polytungstic structure (Fig. 4a) [36]. It should be noted that the Keggin structure bands completely disappeared. On the other hand, SiO_2 support showed typical vibration at 794 and 476 cm^{-1} [37]. Raman spectrum of HPW/SiO_2 catalyst displayed bulk WO_3 bands (Fig. 4b) [38].

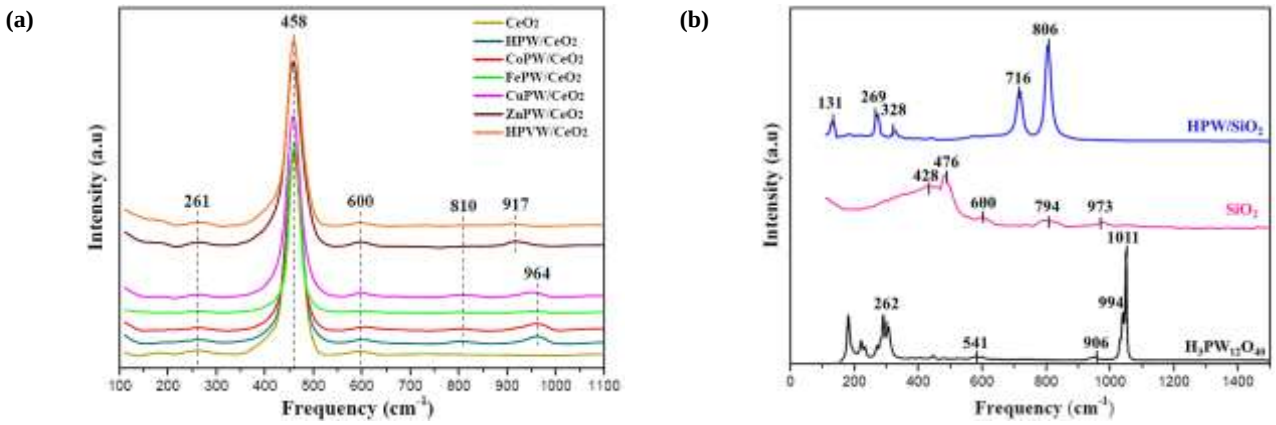

Fig. 4 Raman spectra of **(a)** CeO_2, MPW/CeO_2 (M= Co, Fe, Cu, Zn), HPVW/CeO_2, and **(b)** SiO_2, HPW/SiO_2

In order to understand how the supports were affected by POMs addition, diffuse reflectance UV-Vis spectroscopy was performed. In fact, this technique was used to probe the nature of tungstic species dispersed on the catalyst surface. It was found that each tungsten oxide type diffuses its own energy bandgaps (Eg). The Eg was calculated from the Tauc plot, using O^{2-} to metal charge transfer band (Fig. S7, Table 2). POMs bulk (bandgaps around 3.03-2.5 eV) exhibited energy gaps between the isolate form (Na_2WO_4/ Eg = 4.89 eV) and tungsten oxide (WO_3/ Eg =

2.3 eV) [39]. The use of ceria as a support (Eg = 2.7 eV) decreased the energies of POMs to 2.79- 2.46 eV. In this case, the ceria surface was covered by octahedral [WO_6] and tetragonal [WO_4] tungstic units [40]. Meanwhile, HPW/SiO_2 catalyst showed bandgap at 2.46 eV, which closely approached the energy value of WO_3 particles (Fig. S7b).

Table 2 Energy bandgaps of POMs, supports (CeO_2, SiO_2) and catalysts

Compounds	POMs bandgaps (eV)	supports	Catalysts bandgaps (eV)
HPW	3.03	SiO_2 (3.8 eV)	2.36 2.77
CoPW	2.97		2.79
FePW	2.94	CeO_2 (2.7 eV)	2.58
CuPW	3.01		2.63
ZnPW	3.02		2.61
HPVW	2.50		2.46

Fig. S8 depicts the deconvoluted XPS spectra of CeO_2, HPW/CeO_2 and CoPW/CeO_2 in spectral regions of Ce 3d, O 1s and W 4f. As described in the literature, Ce 3d displays the binding energies at 882.5, 889.2, 898.7, 901.2, 907.5 and 917.2 eV, which are attributed Ce^{4+}, while the peaks at 885.5 and 903.6 eV are ascribed to Ce^{3+} [12]. The peak centered around 37.7 and 35.8 eV are associated respectively to W $4f_{5/2}$ and W $4f_{7/2}$ of W^{6+} [41]. For O 1s, the peaks appearing at 532.6 and 529.9 eV are assigned to surface lattice oxygen (O_α) and surface adsorbed oxygen (O_β) respectively [42]. The surface proportion of Ce^{3+} ($Ce^{3+}/(Ce^{3+} + Ce^{4+})$) over ceria was determined to be 12.78% (Table S3). After the grafting of HPW and CoPW, the amount of Ce^{3+} increased significantly to 17.47% and 28.96%, respectively. The obtained results suggest the presence of more oxygen vacancies on the catalysts surface. In the O 1s spectra, the estimated relative amounts of O_α were 34, 30 and 20% for CeO_2, HPW/CeO_2 and CoPW/CeO_2, respectively. The decrease in lattice oxygen on the surface of the catalysts may be attributed to its interaction with the supported tungsten, confirming the existence of oxygen vacancies suggested previously [43].

3.2 Catalytic activity

3.2.1 Support effect

Catalytic activity of silica and ceria supported HPW in SCR at different temperatures is depicted in Fig. 5 and Fig. S9. Unsupported HPW is not active in NH_3-SCR reaction; it did not show any ability to reduce NO in operating temperatures (Fig. S9). Silica (SiO_2) showed a poor catalytic performance (5% NO conversion at 300°C). Meanwhile, ceria performed a little better than silica but with a NO_x conversion only approaching 30% at 400 °C. Compared to silica support catalyst, HPW/CeO_2 remarkably performed. The catalytic activity over this catalyst showed 98% NO_x conversion and 99% N_2 selectivity within 280−450 °C temperature range. For both catalysts, very low amounts of N_2O were formed during the whole reduction process, with a maximum value recorded at 400 °C over HPW/SiO_2 (Fig. S10).

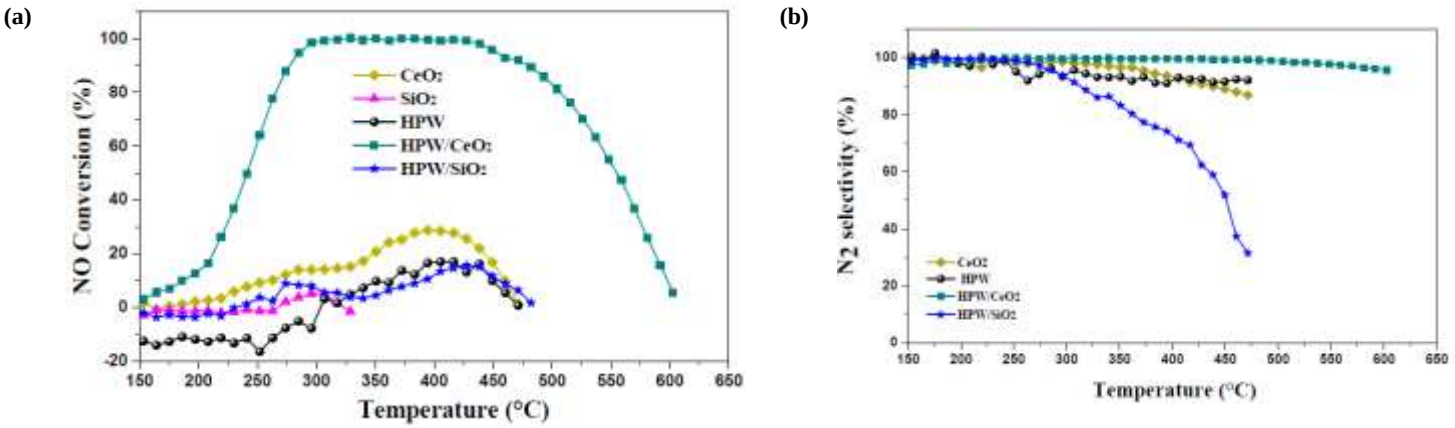

Fig. 5 Catalytic performance (**(a)** NO_x conversion, **(b)** N_2 selectivity) of SiO_2, CeO_2, HPW/CeO_2 and HPW/SiO_2 catalysts. Operation conditions: $[NH_3]$ = 350 ppm, [NO] = 300 ppm and GHSV = 30000 h^{-1}

3.2.2 Proton exchange effect

HPW/CeO_2, the most active catalyst, has been carefully examined in SCR activity. The effect of cationic substitution of proton was analyzed in SCR reaction using Co^{2+}, Fe^{2+}, Cu^{2+}, Zn^{2+} exchangers Fig. 6). The highest deNO_x efficiency was obtained with Co-modified HPW, more than 98% of NO_x conversion of the temperature range 280-500 °C was observed. Overall results showed that SCR activity decreased in the order: Co > H > Zn > Cu > Fe. Moreover, a similar trend was detected for NO_2 production (Fig. S11).

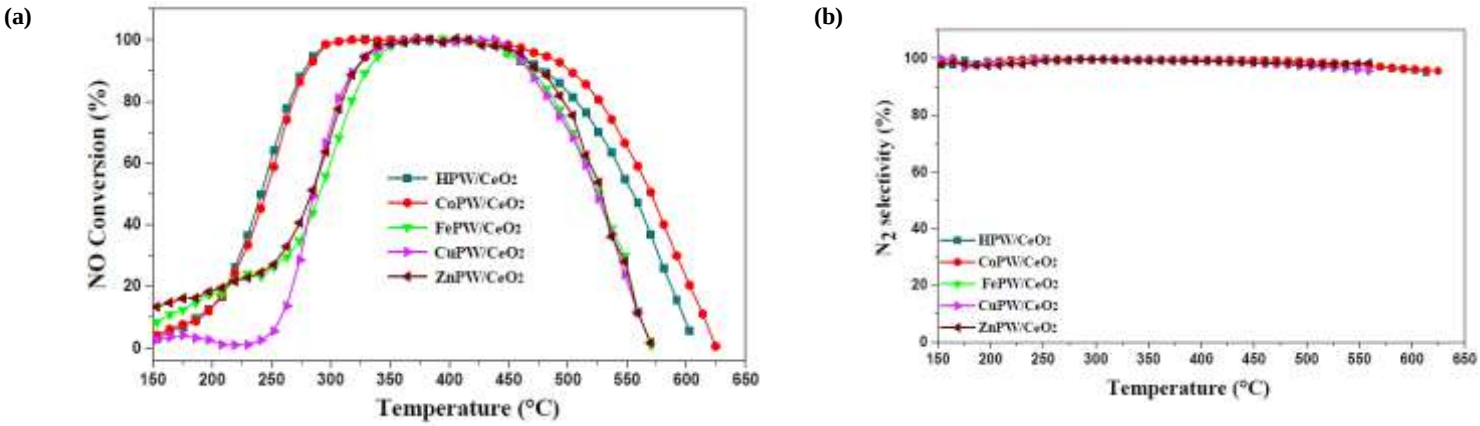

Fig. 6 Catalytic performance (**(a)** NO_x conversion, **(b)** N_2 selectivity) of HPW/CeO_2, MPW/CeO_2 (M = Co, Fe, Cu, Zn) catalysts. Operation conditions: $[NH_3]$ = 350 ppm, [NO] = 300 ppm and GHSV = 30,000 h^{-1}

3.2.3 Tungsten exchange effect

The second component analyzed in HPW/CeO_2 for SCR is the tungsten through a substitution of W^{VI} with V^{V}. The catalytic performance is shown in Fig. 7. It can be seen that the catalytic activity of $HPVW/CeO_2$ was lower than that of HPW/CeO_2 catalyst. $HPVW/CeO_2$ removed around 88 % of NO_x at 320 °C. For temperatures above 320°C, NO reduction process slows down and N_2O concentration increases (Fig. S12).

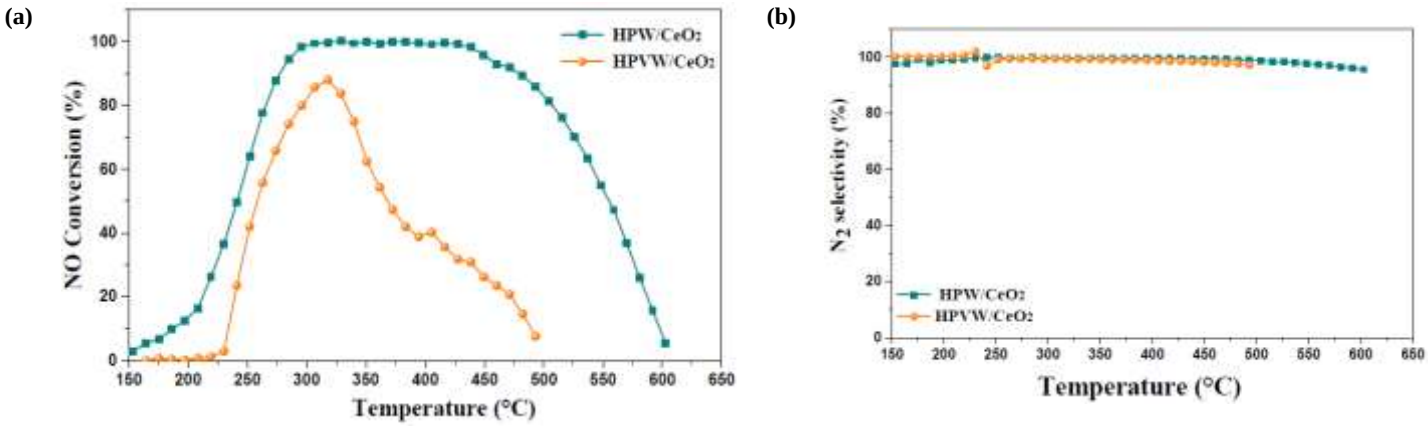

Fig. 7. Catalytic performance (**(a)** NO_x conversion, **(b)** N_2 selectivity) of HPW/CeO_2 and $HPVW/CeO_2$ catalysts. Operation conditions: $[NH_3]$ = 350 ppm, [NO] = 300 ppm and GHSV = 30,000 h^{-1}

4 Discussion of the Results

The catalytic performances of HPW in the selective catalytic reduction of NO with NH_3 depend on the support material and then on the nature of the promoter introduced. Catalytic activity was linked to the formation of surface active species generated from the HPW precursor and to their dispersion capacity. The ceria, due to its reducibility, could be favorable to the production of oxygen vacancies, the latter are necessary in the process of interaction between HPW and support. The HPW/CeO_2 catalyst revealed the presence of tungstic monomer and polymer species. On the other hand, HPW/SiO_2 only produced WO_3 particles (Fig. 8a) which had a limited activity in the SCR reaction. Tungstic oxides species likely produced by the degradation of HPW keggin structure (confirmed by XRD (Fig. 3), IR (Fig. 4), Raman (Fig. 5) and UV-Vis (Fig. S7)) consisted in monomeric (WO_4) and polytungstic (WO_5/WO_6) fragments. Tungstic oxides had a control on the surface acidity providing the appropriate combination of Bronsted and Lewis acid sites as reported elsewhere [40,44]. Regarding the effect of the HPW precursor on the deNO_x performance, redox property of HPW/CeO_2 related to the availability of oxygen vacancies in ceria network may explain the activity of the catalyst. Raman spectra (Fig. 4, Table 1) showed that the amounts of oxygen vacancies on HPW/CeO_2 catalysts were significantly higher compared to those on ceria support. Therefore, the formation of acidic sites on the catalytic surface resulted in stronger adsorption of NH_3, inducing an easy reduction of absorbed NO. At structural level, it was found that the interaction between ceria and monomeric or polymeric tungsten produced $W(=O)(O\text{-}Ce)_4$ and $W(=O)_3(O\text{-}Ce)_4$ species on the surface, respectively (Fig. 8b and c). The isolated $W(=O)(O\text{-}Ce)_4$ form was active at high temperature, while, the oligomeric $W(=O)_3(O\text{-}Ce)_4$ species performed at low temperature [45]. The HPW/CeO_2 surface is covered by both forms, resulting in a better performance at broad operating temperature window (280–450 °C).

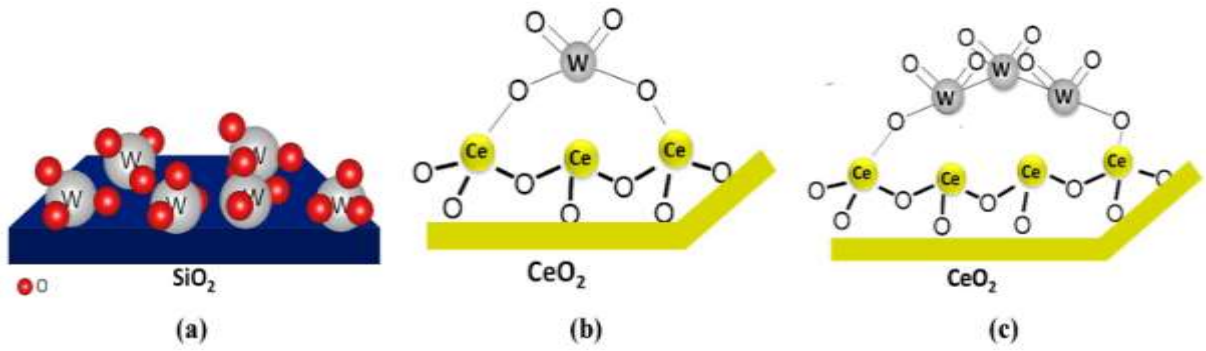

Fig. 8 Proposed structure of (a) WO_3 nanoparticles on SiO_2, (b) monomeric and (c) polymeric tungsten on CeO_2

HPW was more effective when supported on ceria and promoted by cobalt for SCR reaction in a wide temperature range. At 300 and 500 °C, NO_x yield on tested catalysts was closely correlated to tungsten dispersion capacity, oxygen vacancies and metal incorporated (Fig. 9). $CoPW/CeO_2$ had a great dispersion capacity and a high oxygen vacancies formation. Furthermore, it is suggested that the cobalt-ceria interaction improves the formation of intermediate nitrogenous species [46]. Using X-ray photoemission, X-ray absorption, and thermal desorption spectroscopy experiments, several N_xO_y species (nitrosyl anion (NO^-), nitrate ion (NO^{3-}) and hyponitrite anion (N_2O_2)) are observed on the ceria surface, which have been reported to be essential for NO_x removal in NH_3-SCR process [47,48]. The promoting effect of cobalt led to the highest deNO_x performance obtained on $CoPW/CeO_2$. The catalyst surface acidity effect on the SCR performance has been checked using the substitution of tungsten by vanadium into HPW. As noticed, deNO_x efficiency was significantly affected. The addition of V led to a decrease in acidity of HPW with a lower number of acid sites on the ceria surface [18].

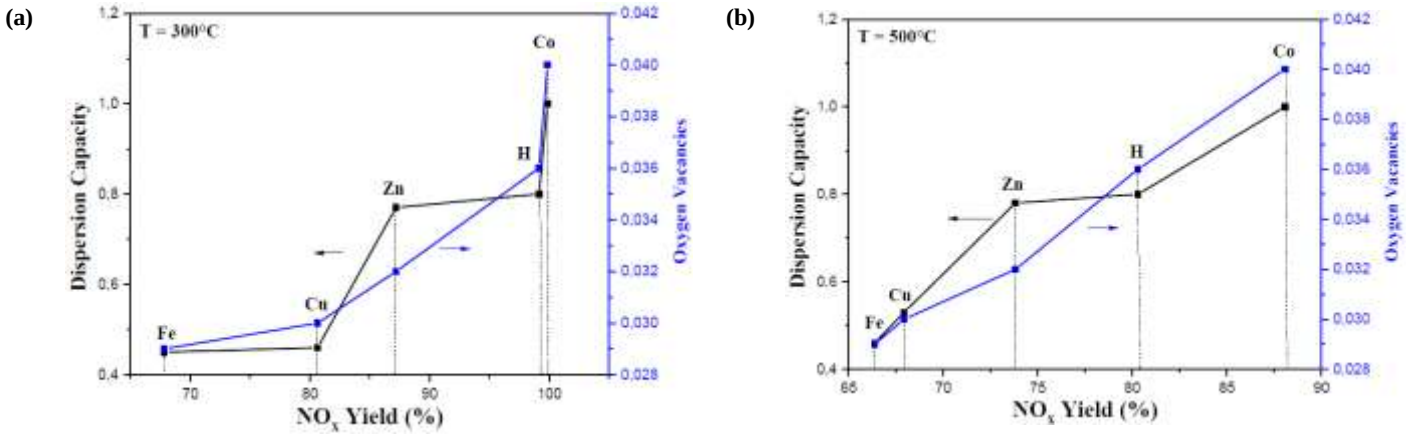

Fig. 9 Contributions of dispersion capacity and oxygen vacancies in $MHPW/CeO_2$ (M = H, Co, Fe, Cu and Zn) catalysts to NO_x yield at **(a)** 300 °C and **(b)** 500°C

The relationship between catalytic performance and the catalyst properties in SCR process are supported by kinetic investigation carried out at differential regime operative conditions (Fig. 10). The catalysts activation energies increased as follows: $CoPW/CeO_2$ (45 kJ. mol^{-1}) > HPW/CeO_2 (48 kJ. mol^{-1}) > $ZnPW/CeO_2$ (55 kJ. mol^{-1}) > $CuPW/CeO_2$ (66 kJ. mol^{-1}) > $FePW/CeO_2$ (78 kJ. mol^{-1}) > $HPVW/CeO_2$ (183 kJ. mol^{-1}) > HPW/SiO_2 (238 kJ. mol^{-1}). The kinetic results are in accordance with SCR activity previously reported.

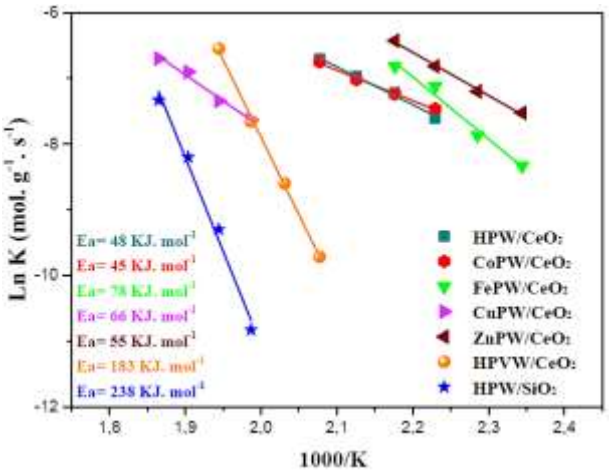

Fig. 10. Arrhenius plot for NH_3-SCR reaction over HPW/CeO_2, MPW/CeO_2 (M = Co, Fe, Cu, Zn), $HPVW/CeO_2$ and HPW/SiO_2 catalysts

Table S4 displays some representative data of SCR activity for various catalysts based on tungsten and ceria support reported from recent studies and the catalysts tested in this work. Both systems HPW/CeO_2 and $CoPW/CeO_2$ developed in this study shows that adding only a small amount of tungsten to ceria support is enough to achieve a NO conversion of 98% with 99% N_2 selectivity and an SCR activity of 0.73 $mol_{NO}.g_{cat}^{-1}.s^{-1}$. The catalysts turn out to be more active than other $deNO_x$ converters recently reported: commercial catalyst 5% V_2O_5-WO_3/TiO_2 [22], $HPW/CeO_{2\text{-}500}$ (W = 50%) catalyst [22], and $W(\equiv C\textit{t}Bu)(CH_2\textit{t}Bu)_3/CeO_2$ (W = 9%) precatalyst [43].

5 Conclusion

Supported POMs-based catalysts were prepared by wet impregnation technique and analyzed by N_2 adsorption-desorption, SEM, XRD, FT-IR, Raman, UV-Vis and XPS spectroscopies for further testing in $deNO_x$ reaction.
HPW associated with ceria displayed an excellent NO_x conversion compared with silica. The synergy effect between ceria and tungsten (from HPW degradation) enhanced the reducibility and the acidity at catalyst surface. In contrast, the silica support favored WO_3 particles formation in HPW/SiO_2 framework, leading to a limited activity in SCR reaction over this catalyst.
For $CoPW/CeO_2$ catalyst, an outstanding NO_x conversion across the temperature 280-500°C range was obtained. The remarkable behavior of Co-incorporated HPW/CeO_2 is related to the high dispersion capacity and to the oxygen vacancies of ceria support which favored the adsorption and subsequently the activation of reactants (NH_3 and NO). Meanwhile, cobalt-ceria interaction promotes the intermediate nitrogenous species, resulting in relatively higher performance at a medium-high temperature.
Substitution of tungsten by vanadium decreased HPW acidity, $HPVW/CeO_2$, displayed lower performance for NO_x abatement.

Supplementary Information See below. The online version also contains a link to the supplementary material, available on the journal Web site.

Acknowledgements This work is financially supported by the R&D Initiative-APPHOS-OCP (OCP Foundation, R&D OCP, Mohammed VI Polytechnic University, National Center of Scientific and technical

Research CNRST, Ministry of Higher Education, Scientific Research and Professional Training of Morocco MESRSFC) under the project ID * CHF-OUL-01/2017 and by the "Centre National de la Recherche Scientifique" (CNRS, France).

Conflict of interest The authors declare no conflict of interest

Author Contribution: Imane El Arrouji: Data curation, Writing-original draft. **Kaï Chung Szeto:** Data curation. **Aimery de Mallmann:** Data curation. **Chérif Larabi:** Data curation. **Mostafa Taoufik:** Data curation, Supervision. **Abdallah Oulmekki:** Supervision**,** Writing-review and editing. **Jamil Toyir:** Supervision**,** Writing-review and editing.

References

1. T. Boningari, P.G. Smirniotis, Curr. Opin. Chem. Eng. **13**, 133–141 (2016)
2. L. Han, S. Cai, M. Gao, J. Hasegawa, P. Wang, J. Zhang, L. Shi, D. Zhang, Chem. Rev. **119**, 10916–10976 (2016)
3. F. Prinetto, G. Ghiotti, M. Occhiuzzi, V. Indovina, J. Phys. Chem. B. **102**, 10316–10325 (1998)
4. S. Liu, H. Wang, Y. Wei, R. Zhang, S. Royer, ACS Appl. Mater. Interfaces. **11**, 22240–22254 (2019)
5. B. Shen, Y. Wang, F. Wang, T. Liu, Chem. Eng. J. **236**, 171–180 (2014)
6. H. Chang, X. Chen, J. Li, L. Ma, C. Wang, C. Liu, J.W. Schwank, J. Hao, Environ. Sci. Technol. **47**, 5294–5301 (2013)
7. W. Shan, Y. Yu, Y. Zhang, G. He, Y. Peng, J. Li, H. He Catal. Today **376**, 292–301 (2021)
8. A. Wang, Y. Wang, E.D. Walter, N.M. Washton, Y. Guo, G. Lu, C.H.F. Peden, F. Gao, Catal. Today. **320**, 91–99 (2019)
9. Q. Jin, Y. Shen, S. Zhu, H. Li, Y. Li, J. Mater. Res. **32**, 2439 (2017)
10. F. Gao, X. Tang, H. Yi, S. Zhao, C. Li, J. Li, Y. Shi, X. Meng, Catalysts. **7**, 199 (2017)
11. A. Trovarelli, Comments Inorg. Chem. **20**, 263–284 (1999)
12. S. Yang, Y. Guo, H. Chang, L. Ma, Y. Peng, Z. Qu, N. Yan, C. Wang, J. Li, Appl. Catal. B Environ. **136**, 19–28 (2013)
13. T. Gu, Y. Liu, X. Weng, H. Wang, Z. Wu, Catal. Commun. **12**, 310–313 (2010)
14. S. Zhan, H. Zhang, Y. Zhang, Q. Shi, Y. Li, X. Li, Appl. Catal. B Environ. **203**,199–209 (2017)
15. H. Xu, M. Sun, S. Liu, Y. Li, J. Wang, Y. Chen, RSC Adv. **7**, 24177–24187 (2017)
16. Y. Geng, W. Shan, S. Xiong, Y. Liao, S. Yang, F. Liu, Catal. Sci. Technol. **6**, 3149–3155 (2016)
17. Z. Liu, J. Zhu, J. Li, L. Ma, S.I. Woo, ACS Appl. Mater. Interfaces. **6**, 14500–14508 (2014)
18. A. Müller, M.T. Pope, Kluwer Academic Publishers, (2001)
19. I. El Arrouji, A. Oulmekki, M. Taoufik, F. Lefebvre, J. Toyir, Mater. Today: Proc. **51**, 2015-2021 (2022)
20. Y. Geng, S. Xiong, B. Li, Y. Peng, S. Yang, Ind. Eng. Chem. Res. **57**, 13661–13670 (2018)
21. Y. Ke, W. Huang, S. Li, Y. Liao, J. Li, Z. Qu, N. Yan, Catal. Sci. Technol. **9**, 5774–5785 (2019)
22. Y. Geng, S. Xiong, B. Li, Y. Liao, X. Xiao, S. Yang, Ind. Eng. Chem. Res. **57**, 856–866 (2018)
23. Y. Geng, K. Jin, J. Mei, G. Su, L. Ma, S. Yang, J. Hazard. Mater. **382**, 121032 (2020)
24. X. Tong, N. Tian, W. Zhu, Q. Wu, F. Cao, W. Yan, J. Alloys Compd. **544**, 37–41 (2012)
25. A. Aouissi, S.S. Al-deyab, A. Al-owais, A. Al-amro, Int. J. Mol. Sci. **1**, 1 2770–2779 (2010)

26. S. Gillot, G. Tricot, H. Vezin, J.-P. Dacquin, C. Dujardin, P. Granger, Appl. Catal. B Environ. **218**, 338–348 (2017)
27. Y. Chen, L. Dong, Y.S. Jin, B. Xu, W. J, Stud. Surf. Sci. Catal. 1293–1302 (1996)
28. R. Podor, N. Clavier, J. Ravaux, L. Claparede, N. Dacheux, D. Bernache-Assollant, J. Eur. Ceram. Soc. **32**, 353–362 (2012)
29. I.Y. Kaplin, E.S. Lokteva, E. V Golubina, V. V Lunin, Molecules. **25**, 4242 (2020)
30. V. Ramasamy, V. Mohana, V. Rajendran, OpenNano. **3**, 38–47 (2018)
31. Y. Idrissou, T. Mazari, S. Benadji, M. Hamdi, C. Rabia, React. Kinet. Mech. Catal. **119**, 291–304 (2016)
32. D.S. Kim, M. Ostromecki, I.E. Wachs, S.D. Kohler, J.G. Ekerdt, Catal. Letters. **33**, 209–215 (1995)
33. A.M.D. de Farias, D. Nguyen-Thanh, M.A. Fraga, Appl. Catal. B Environ. **93**, 250–258 (2010)
34. X. Wang, G. Lu, Y. Guo, Y. Xue, L. Jiang, Y. Guo, Z. Zhang, Catal. Today. **126**, 412–419 (2007)
35. C. Bigey, L. Hilaire, G. Maire, J. Catal. **198**, 208–222 (2001)
36. I.E. Wachs, T. Kim, E.I. Ross, Catal. Today. **116**, 162–168 (2006)
37. M. Ivanda, R. Clasen, M. Hornfeck, W. Kiefer, J. Non. Cryst. Solids. **322**, 46–52 (2003)
38. H. Yoon, M.G. Mali, M. Kim, S.S. Al-Deyab, S.S. Yoon, Catal. Today. **260**, 89–94 (2016)
39. J.G. Howell, Y.-P. Li, A.T. Bell, ACS Catal. **6**, 7728–7738 (2016)
40. Z. Ma, D. Weng, X. Wu, Z. Si, J. Environ. Sci. **24**, 1305–1316 (2012)
41. R. M. Ladera, M. Ojeda, J. L. G. Fierro, S. Rojas, Catal. Sci. Technol. **5**, 484–491 (2015)
42. J. Mei, Y. Ke, Z. Yu, X. Hu, Z. Qu, N. Yan, Chem. Eng. J. **320**, 124–134 (2017)
43. C. Larabi, C. Chen, N. Merle, M. Charlin, K. C. Szeto, A. De Mallmann, A. Benayad, K. Ben Tayeb, A. Kaddouri, H. P. Nguyen, M. Taoufik, New J. Chem. **45**, 12024–12032 (2021)
44. Y. Peng, K. Li, J. Li, Appl. Catal. B Environ. **140**, 483–492 (2013)
45. I. El Arrouji, C. Chen, J. Toyir, C. Larabi, K. C. Szeto, A. De Mallmann, M. Taoufik, A. Oulmekki, Catalysts **11**, 950 (2021)
46. V.G. Milt, C.A. Querini, E.E. Miró, M.A. Ulla, J. Catal. **220**, 424–432 (2003)
47. N. Akter, S. Zhang, J. Lee, D.H. Kim, J.A. Boscoboinik, T. Kim, Mol. Catal. **482**, 110–664 (2020)
48. S.H. Overbury, D.R. Mullins, D.R. Huntley, L. Kundakovic, J. Catal. **186**, 296–309 (1999)

GRAPHICAL ABSTRACT

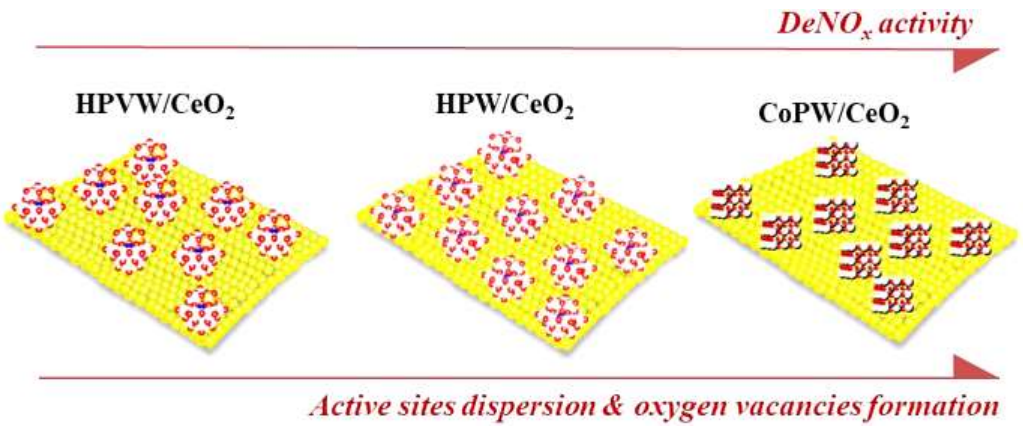

SUPPORTING INFORMATION

EDX

Table S1 Elemental analysis of CeO_2, SiO_2 and catalysts by EDX

catalysts	Weight percentage		
	Ce	Si	W
CeO_2	80.74	-	-
SiO_2	-	47.14	-
HPW/SiO_2	-	39.77	8.62
HPW/CeO_2	74.05	-	7.96
CoPW/CeO_2	70.65	-	8.94
FePW/CeO_2	72.8	-	8.21
CuPW/CeO_2	74.25	-	8.1
ZnPW/CeO_2	70.63	-	9.74
HPVW/CeO_2	70.52	-	9.3

BET

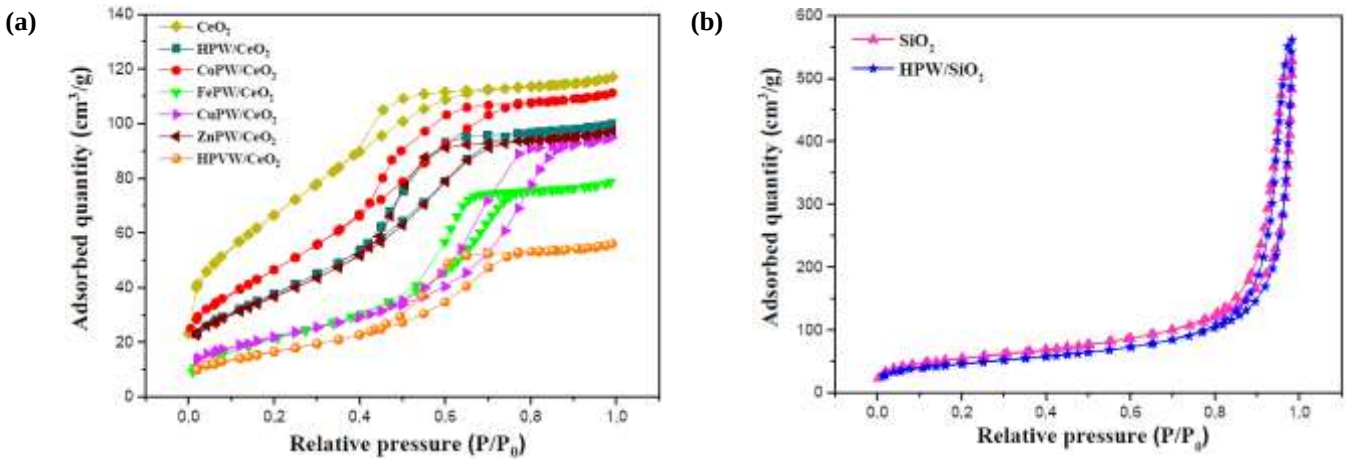

Fig. S1 Physisorption isotherms of **(a)** CeO_2, MPW/CeO_2 (M= Co, Fe, Cu, Zn), HPVW/CeO_2 and **(b)** SiO_2, HPW/SiO_2. Catalysts were outgassed at 200 °C for 4h

MEB

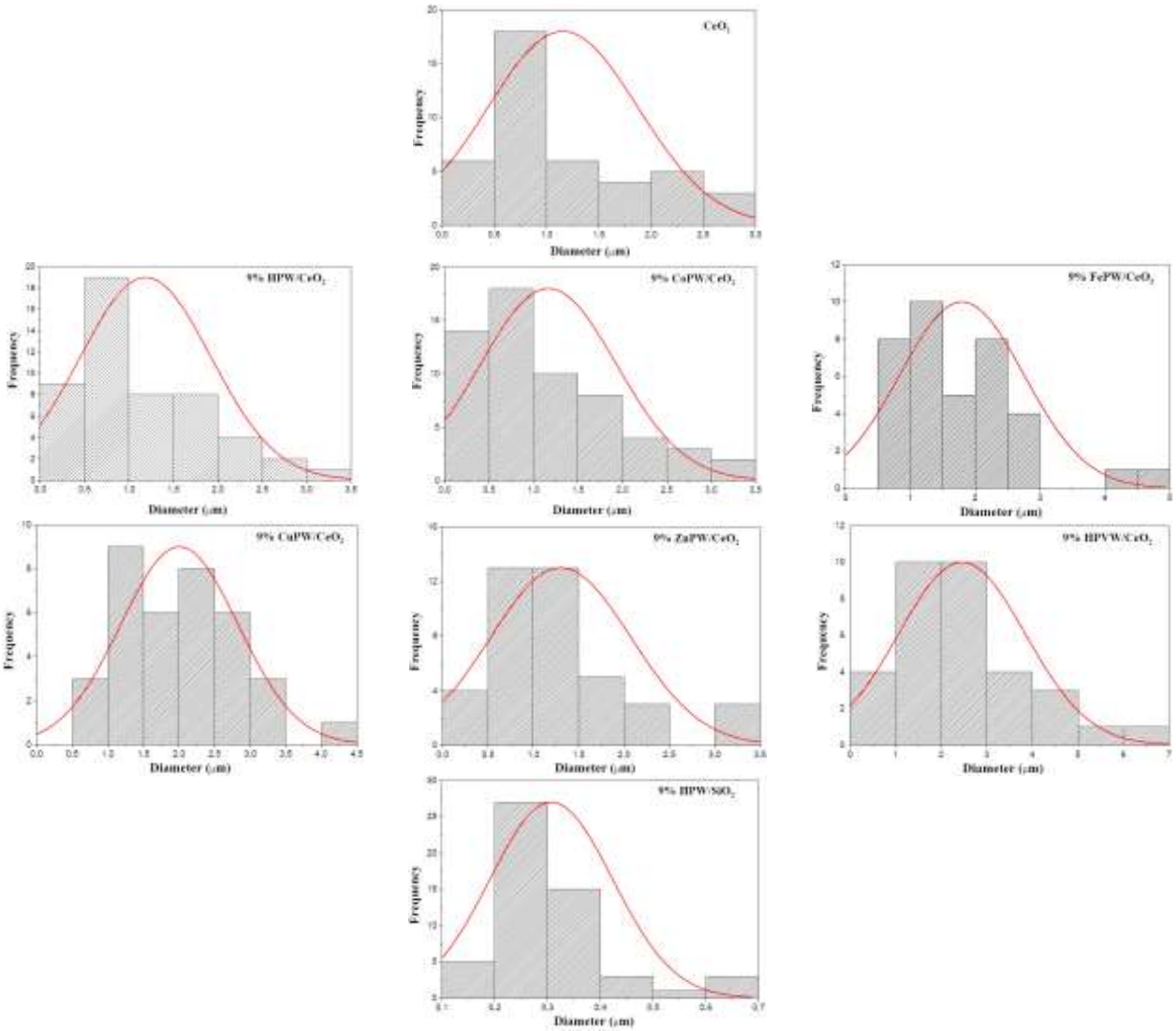

Fig. S2 Size distribution of grains corresponding to samples CeO_2, MPW/CeO_2 (M= H, Co, Fe, Cu, Zn), HPVW/CeO_2, SiO_2 and HPW/SiO_2

XRD

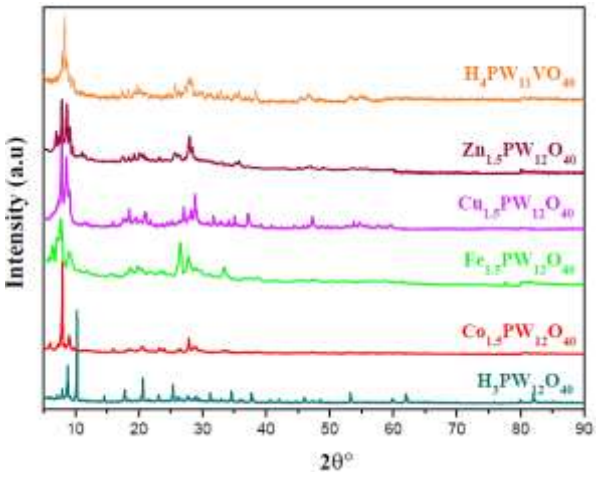

Fig. S3 X-ray diffraction spectra of POMs

CeO_2

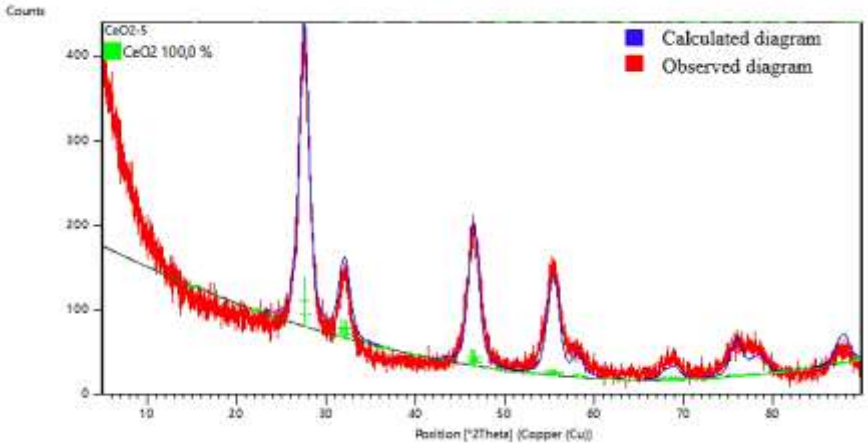

HPW/CeO_2

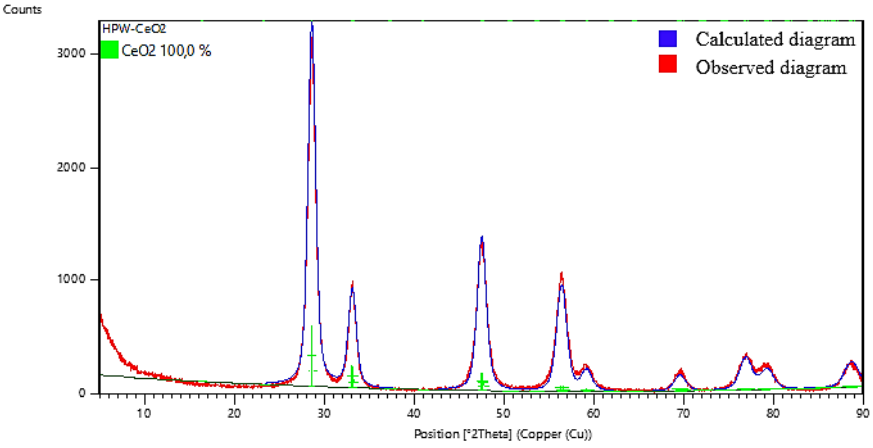

CoPW/CeO_2

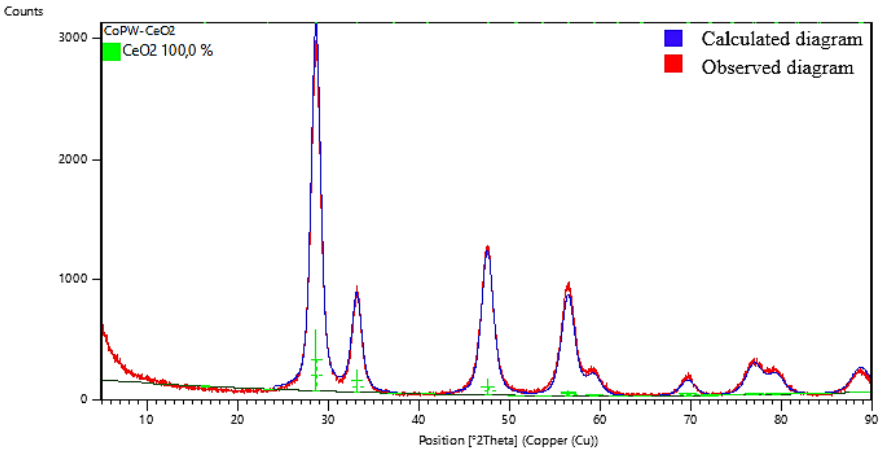

FePW/CeO$_2$

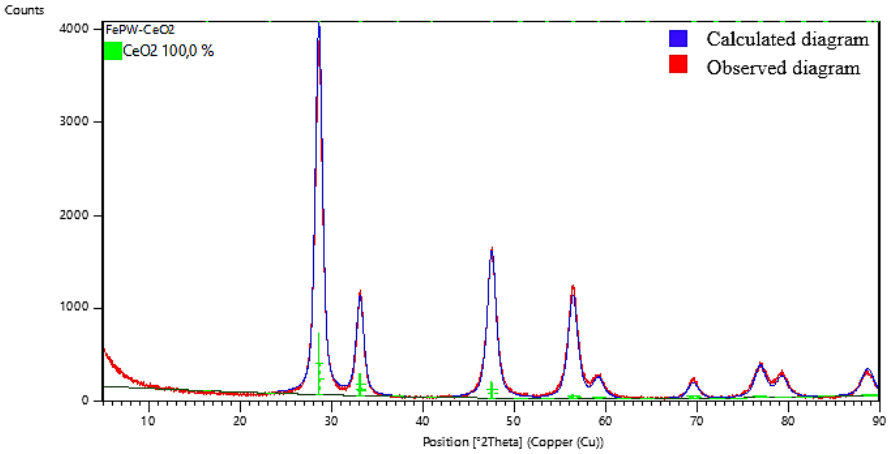

CuPW/CeO$_2$

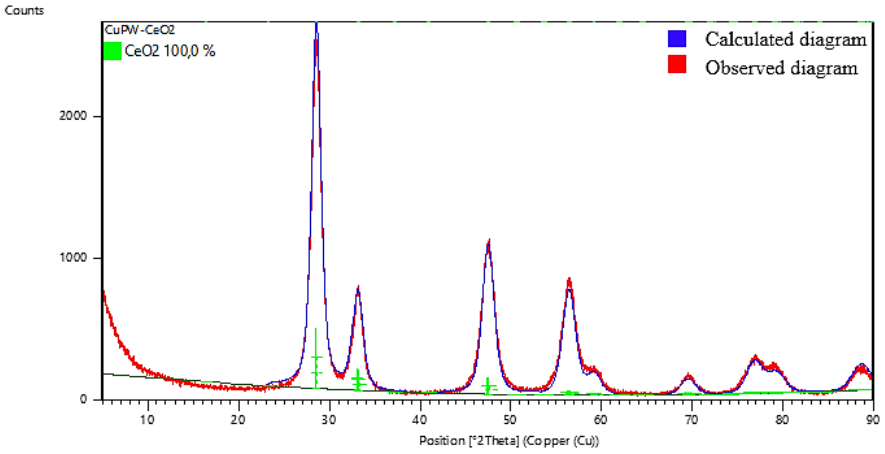

ZnPW/CeO$_2$

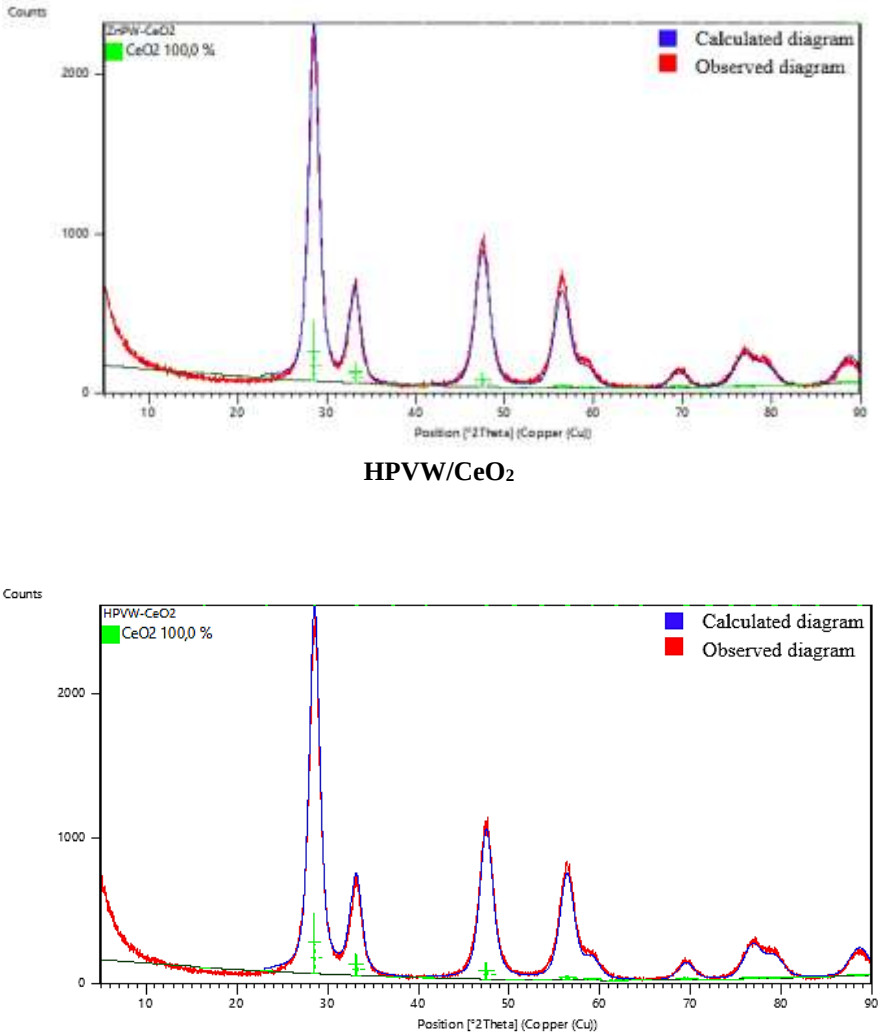

Fig. S4 X-ray diffraction data refinement for CeO_2 and catalysts powders

Table S2 Crystallographic parameters of CeO_2, HPW/CeO_2, MPW/CeO_2 (M= Co, Fe, Cu, Zn) and $HPVW/CeO_2$

Catalysts	Crystal structure	Space group	Parameter (a/ Å)	Volume ($Å^3$)
CeO_2	Cubic	Fm-3m	5.39	157.14
HPW/CeO_2			5.41	158
$CoPW/ CeO_2$			5.4	157.74
$FePW/ CeO_2$			5.4	158
$CuPW/ CeO_2$			5.41	158
$ZnPW/ CeO_2$			5.4	157.74
$HPWV/CeO_2$			5.4	158.24

FT-IR

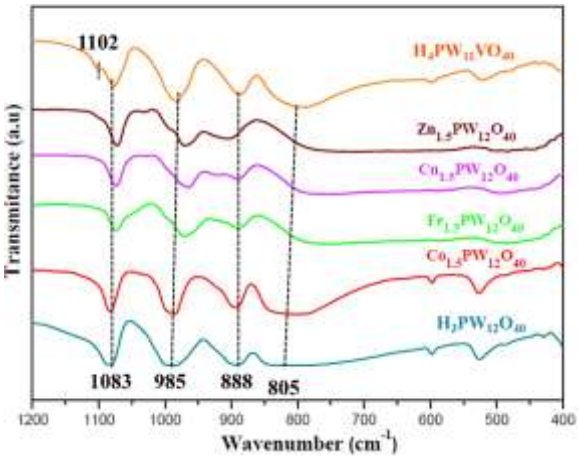

Fig. S5 FT-IR spectra of POM precursors

Raman

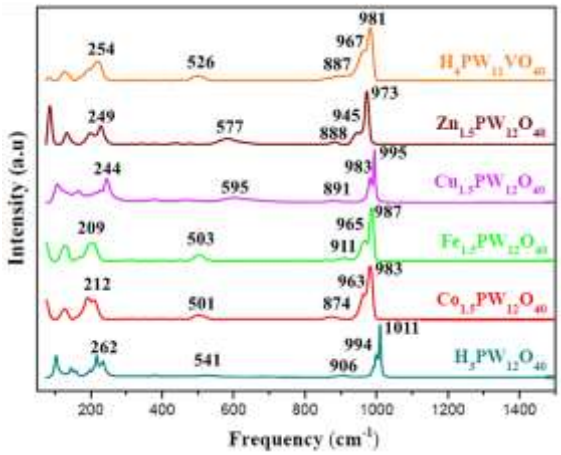

Fig. S6 Raman spectra of POM precursors

UV-Vis

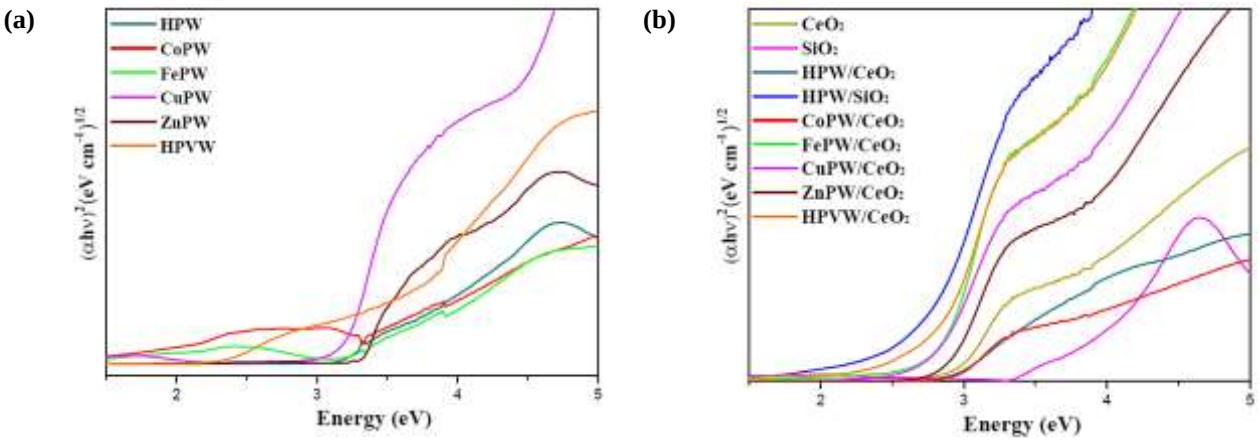

Fig. S7 Tauc plots for **(a)** POMs and **(b)** CeO_2, MPW/CeO_2 (M= Co, Fe, Cu, Zn), HPVW/CeO_2, SiO_2, HPW/SiO_2

XPS

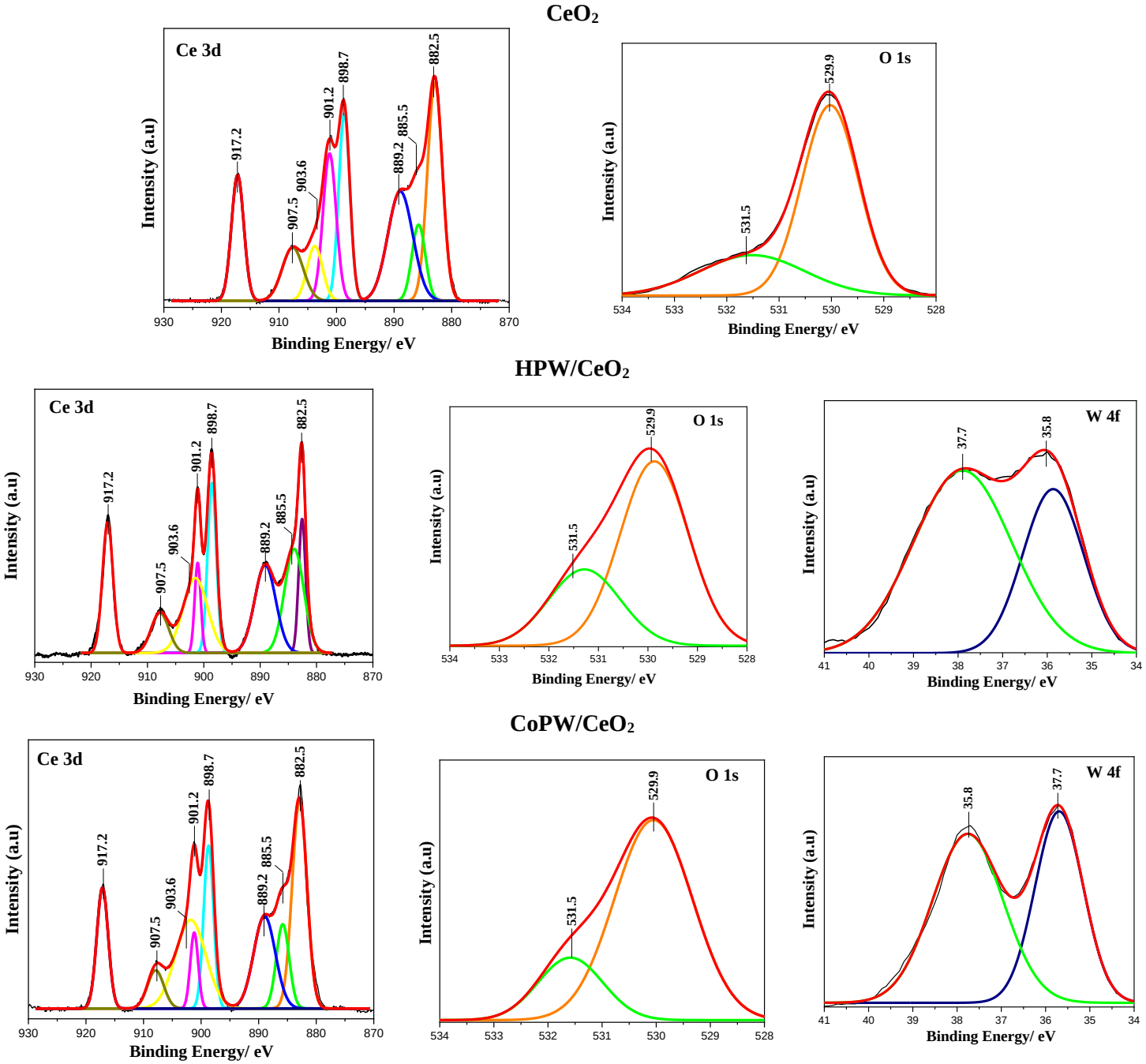

Fig. S8 XPS spectra of Ce 3d, O 1s and W 4f for the catalysts CeO_2, HPW/CeO_2, $CoPW/CeO_2$.

Table S3 XPS surface atomic composition of calcined samples CeO_2, HPW/CeO_2 and HPW/CeO_2

Compounds	Surface atomic (%)	
	$Ce^{3+}/(Ce^{4+} + Ce^{3+})$ %	$O_\alpha/(O_\alpha + O_\beta)$ %
CeO_2	12.78	34
HPW/CeO_2	17.47	30
$CoPW/CeO_2$	28.96	20

Catalytic activity

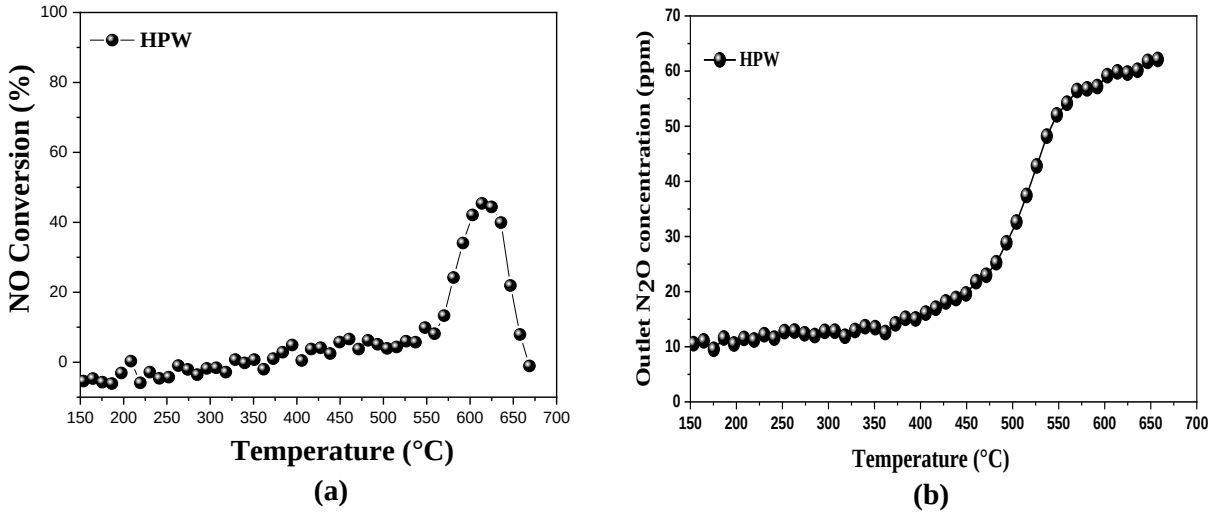

Fig. S9 NO conversion **(a)** and N_2O concentration **(b)** of HPW. Operation conditions: [NH_3] = 350 ppm, [NO] = 300 ppm and GHSV = 30000 h^{-1}

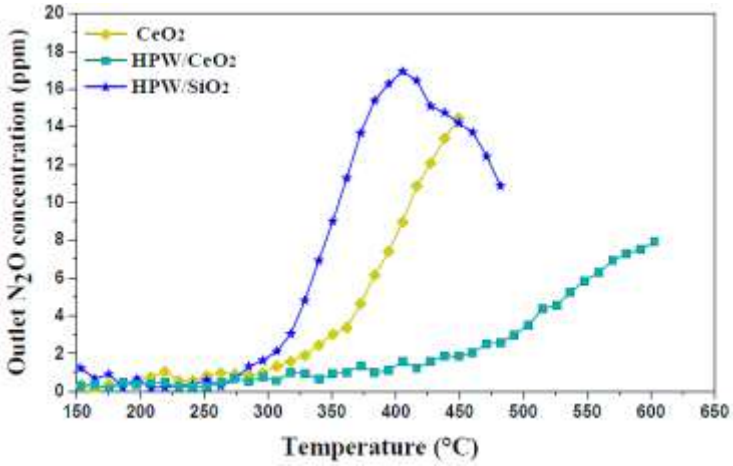

Fig. S10 N_2O concentration observed with CeO_2, HPW/CeO_2 and HPW/SiO_2 catalysts. Operation conditions: [NH_3] = 350 ppm, [NO] = 300 ppm and GHSV = 30000 h^{-1}

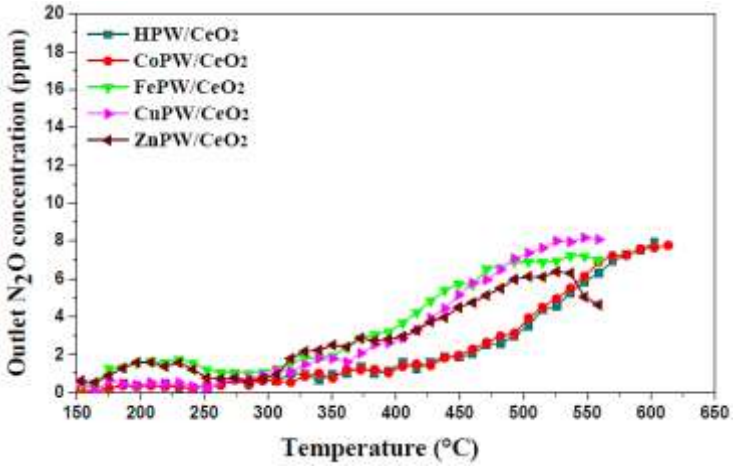

Fig. S11 N_2O concentration of HPW/CeO_2, MPW/CeO_2 (M = Co, Fe, Cu, Zn) catalysts. Operation conditions: [NH_3] = 350 ppm, [NO] = 300 ppm and GHSV = 30000 h^{-1}

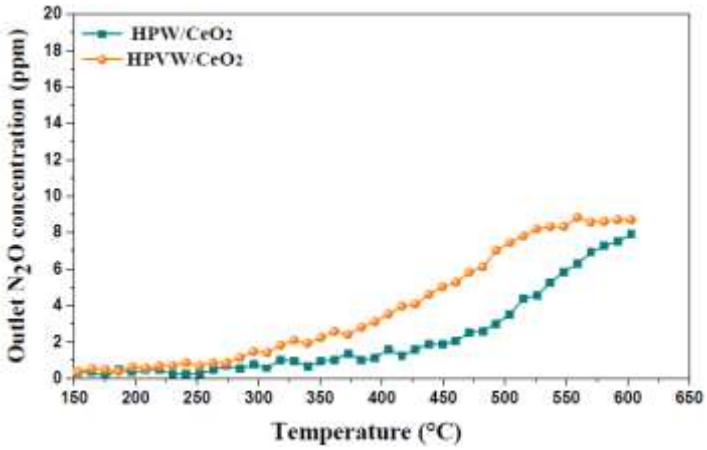

Fig. S12 N_2O concentration of HPW/CeO_2 and $HPVW/CeO_2$ catalysts. Operation conditions: $[NH_3]$ = 350 ppm, [NO] = 300 ppm and GHSV = 30000 h^{-1}

Table S4 A comparison of ceria-tungsten based catalysts used to perform NH_3-SCR reaction.

Catalysts	Conditions	Activity [1] (mol $_{NO}$ g^{-1}_{cat} s^{-1})	N_2 selectivity (%)	Refs
HPW/CeO_2-500 (W = 50%)	[NO] = 500 ppm / $[NH_3]$ = 500 ppm/ m_{cat}= 100 mg F = 200 ml min^{-1}	0.134 (T = 300-450°C)	99	[1]
5% V_2O_5-WO_3/TiO_2		0.134 (T = 300°C)	95	
$W(\equiv CtBu)(CH_2tBu)_3/CeO_2$ (W = 9%)	[NO] = 300 ppm/ $[NH_3]$ = 350 ppm / m_{cat}= 30 mg F = 300 ml min^{-1}	0.707 (T = 280-400°C)	99	[2]
HPW/CeO_2 (W = 9%)		0.730 (T = 280-450°C)	99	This work
$CoPW/CeO_2$ (W = 9%)		0.730 (T = 280-500°C)	99	

[1] SCR activity calculated using following equation: $A\ (mol_{NO} g^{-1}_{cat} s^{-1}) = \frac{X_{NO}\, F}{m_{cat}\ 60\ 22.4}$, where X_{NO} is the maximal conversion, F is the flow rate and m_{cat} is mass of catalyst.

[1] Y. Geng, S. Xiong, B. Li, Y. Liao, X. Xiao, S. Yang. Ind. Eng. Chem. Res. 57 (2018) 856–866.

[2] C. Larabi, C. Chen, N. Merle, M. Charlin, K.C. Szeto, A. De Mallmann, A. Benayad, K. Ben Tayeb, A. Kaddouri, H.P. Nguyen, M. Taoufik.New J. Chem. (2021).